View metadata, citation and similar papers at core.ac.uk
brought to you by CORE
provided by IntechOpen

We are IntechOpen, the world's leading publisher of Open Access books Built by scientists, for scientists

4,800
Open access books available

122,000
International authors and editors

135M
Downloads

154
Countries delivered to

Our authors are among the
TOP 1%
most cited scientists

12.2%
Contributors from top 500 universities

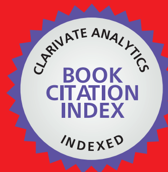

WEB OF SCIENCE™

Selection of our books indexed in the Book Citation Index in Web of Science™ Core Collection (BKCI)

Interested in publishing with us?
Contact book.department@intechopen.com

Numbers displayed above are based on latest data collected.
For more information visit www.intechopen.com

6

Bulk Growth and Characterization of SiC Single Crystal

Lina Ning and Xiaobo Hu
JiaXing University & Shandong University
China

IntechOpen

1. Introduction

Sublimation method was used to grow bulk SiC by J.A. Lely for the first time in 1955 (Lely, 1955). It was improved then by Tairov and Tsvetkov and became the most mature method for bulk SiC growth. In this chapter, we will introduce the growth of hexagonal SiC. Although the bulk growth method is well known and used widely, there are still plenty of details which are different and unique for different groups.
The growth of 4H-SiC is not as stable as that of 6H-SiC. That is to say the growth of 4H-SiC needs a harsh growth conditions. In order to grow high quality 4H polytype, the polytype transition of 4H-SiC single crystals had been studied.
Although single crystals of SiC are commercially available, owing to the specific structures of SiC, there are still some structural defects, such as micropipes, mis-orientations, dislocations, stacking faults, basal plane dislocations, particle inclusions, precipitates and so on, which hinder its applications. So in this chapter we also introduce the recent progress in research of structural defects in 6H-SiC single crystals. Three kinds of typical structural defects in 6H-SiC single crystals were investigated. First, we describe the strain field of a micropipe by the theory of screw dislocation. Stress birefringence images from micropipes with different Burgers vectors have been simulated. The results are compared with polarized optical microscopic observations. Second, elementary screw dislocations were observed by back-reflection synchrotron radiation topography (BRSRT). Based on the reflection geometry, the image of an elementary screw dislocation was simulated. Elementary screw dislocation is a pure screw dislocation with Burger vector lc. Finally, Basal plane bending was detected by high resolution X-ray diffractometry (HRXRD) and transmission synchrotron white-beam x-ray topography (SWBXT).
The observation and investigation of the structural defects helped us to understand their formation mechanisms. This makes it possible for us to further decrease or eventually eliminate them.

2. Bulk growth

All the samples were grown by the sublimation method in our group. The crystal growth procedure has been described in detail elsewhere (Hu et al., 2006). The growth of 6H and 4H polytypes are mainly the same, except for temperature range, growth pressure, seed polarity and also growth process.

2.1 Growth of 4H-SiC

During the sublimation growth process of 4H-SiC, other foreign polytypes nucleated easily since the stacking energies for different SiC polytypes are nearly same. Most of the researchers believed that, it is the growth temperature, the polarity and mis-orientation of the seed that influence the stability of polytypic structure during the growth. Schulze (Norbert et al., 1999) and Straubinger (Straubinger et al., 2001) used different polarity seeds to grow 4H-SiC and found that a stable 4H polytype could be obtained by using the seed with 4H C-face. Further research found that the off-axis C-face seeds with misorientation axis towrads the <11-20> direction are better (Rost et al., 2006) for 4H-SiC growth than other seeds. The defects density decreased with the increase of seed mis-orientation from C-face.

2.2 Polytype transition of 4H-SiC

In this chapter, 4H C-face seeds with an 8° mis-orientation towards [11-20] were used to grow 4H-SiC. In order to make out the relationship between the polytype of the as-grown crystal and the surface morphology, the morphology of as-grown surface and polytype transition of 4H-SiC single crystals had been studied by optical microscopy and Raman spectroscopy.

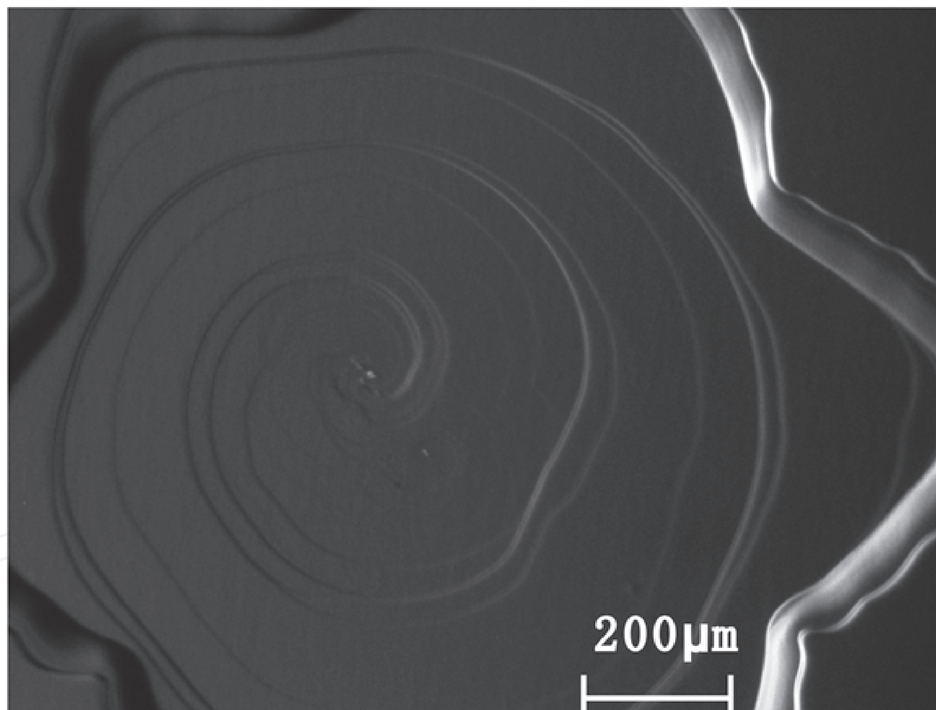

Fig. 1. The morphology of the facet of 4H-SiC

There are two growth mechanisms. Fig. 1 is the morphology of the facet of 4H-SiC. In this region, screw dislocation mechanism controls the growth process. Fig. 2 is the morphology of the area out of the facet. In this region, rough surface growth mechanism dominants. In Fig. 2, there are also two different morphologies. In area A, the growth steps are very fine. In area B, the surface is smooth. There is a slit between the two areas, which is not a scratch caused by machining or annealing after growth. Normally the slit is along the <11-20> direction and extends several or dozens of milli-meters on the as-grown surface.

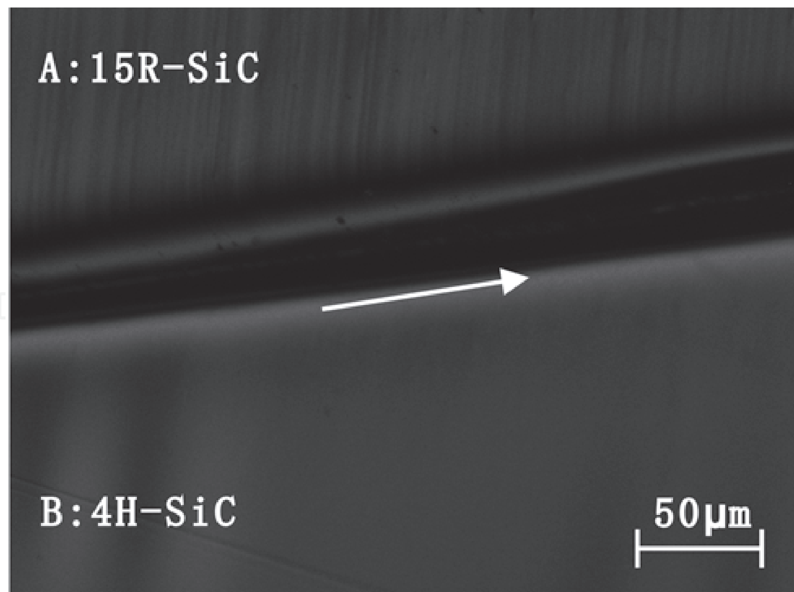

Fig. 2. Micrograph of the as-grown surface showing the existence of 4H-SiC, 15R-SiC at two sides of the slit

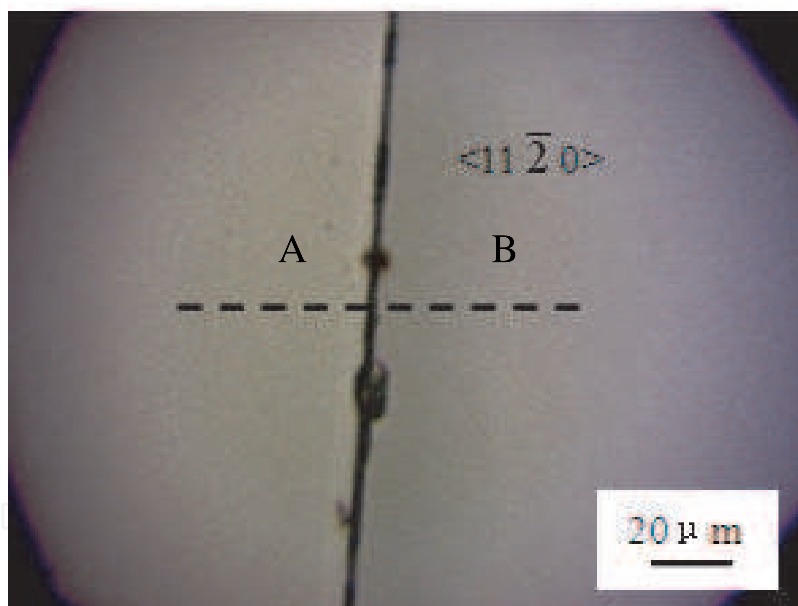

Fig. 3. Schematic diagram of one-dimensional Raman scanning route across the slit

In order to identify the polytype structures in the two areas with different morphologies, Raman spectroscopy were used. One-dimensional Raman scanning was done cross the slit in a range of 100 μm, as shown in Fig. 3.The dashed line represents the scanning path, and the real line is the actual position of slit which is along the <11-20> direction.
The intensity ratio of folded transverse acoustic (FTA) mode of 15R-SiC (Raman shift at 172.3 cm^{-1}) (Wang et al., 2004) and 4H-SiC (Raman shift at 204.99 cm^{-1}) (Wang et al., 2004) was introduced. In Fig. 4, the horizontal coordinate is along the dashed line in Fig. 3, and the longitudinal coordinate is the intensity ratio. According to the intensity ratio, the scanning scope can be divided into three regions. In region A, the intensity ratio is much greater than

one, so it is mainly 15R-SiC whose Raman spectrum is shown in Fig. 5a. In region B, the intensity ratio is much lower than one, so it is mainly 4H-SiC whose Raman spectrum is shown in Fig. 5b. Between the two regions, i.e. near the slit, the intensity ratio drops suddenly. Two points, C and D at a distance of 4μm, were chosen as reference points in this region. The corresponding Raman spectra are shown in Fig. 5c and d.

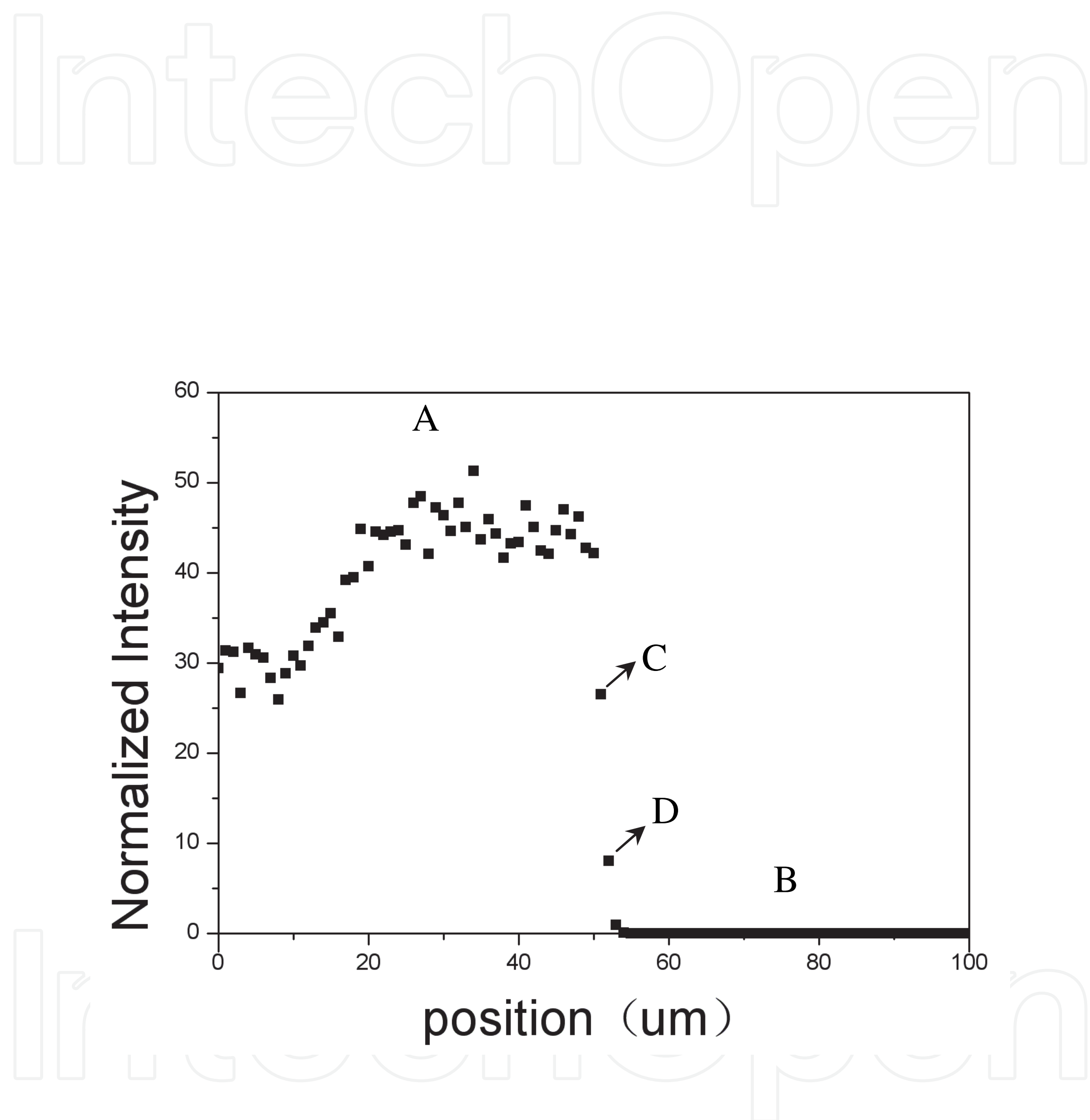

Fig. 4. The intensity ratio of FTA mode along the dashed line in Fig. 3.

From Fig. 5c and 5d, 15R and 4H polytypes appear at the same time. The characteristic peak of 15R-SiC dominates at point C. Both the characteristic peaks of 15R and 4H-SiC are weak and the intensity of the background signal is strong at point D. That is to say, the phonon state density is irregular in this area. In other words, the Si-C di-atom stacking near slit is not completely disorder but contains short range order of 4H and 15R-SiC.

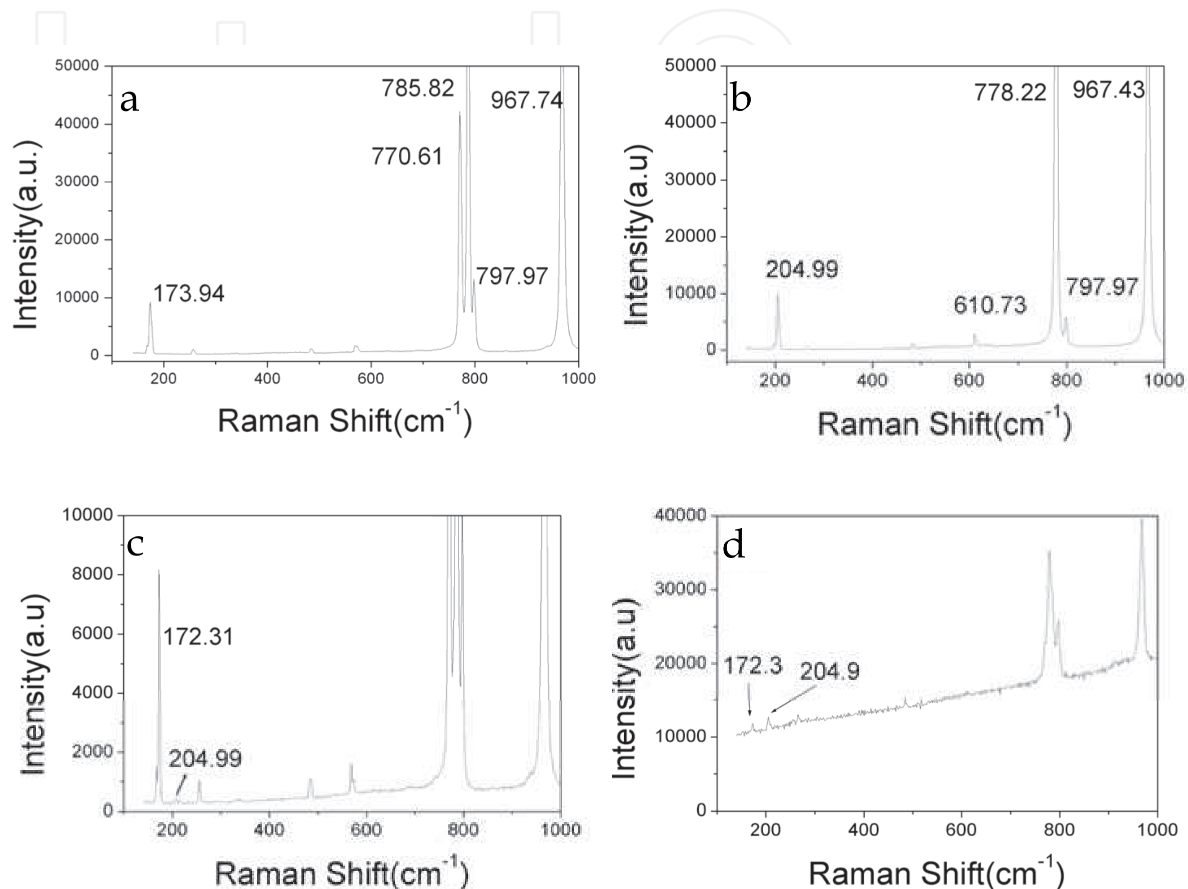

Fig. 5. The Raman spectra at different points of one-dimensional Raman scanning, (a) region A, 15R-SiC; (b) region B, 4H-SiC; (c) point C 15R- and 4H-SiC; (d) point D 4H- and 15R-SiC.

2.3 Summary

In summary, the polytype transition is a process in which the stacking structure changes from long range order to short range order and then back to long range regular. The transition region in our observation is in a range of about 2-3μm. The slit is just the sign of the polytype transition.

3. Characterizations

There are some structure defects in SiC single crystals which hinder its applications. For example, the micropipes increase leakage current and reduce the breakdown voltage of SiC devices (Neudeck & Powell, 1994; Wahab et al., 2000). All the samples used in this section were 6H-SiC wafers grown by sublimation method.

3.1 Micropipes

Hollow tubes called micropipes, which generally run along the c axis, are often found in sublimation grown SiC crystals. There has been much debate regarding the nature of micropipes and several models have been proposed to illuminate the formation mechanism of micropipes. One is based on Frank's theory, which interpreted the formation of micropipes as the stress relaxation of screw dislocations with large Burgers vectors (Frank, 1951). The diameter of micropipes depends on the Burgers vectors of screw dislocations:

$$D = \mu \mathbf{b}^2 / 4\pi\gamma \tag{1}$$

Where D is the core diameter, μ the shear module, **b** the Burgers vector and γ the surface energy. The longer the Burgers vector, the larger is the diameter of the micropipes. The other model suggests that deposition or voids on the growth surface cause the generation of micropipes (Giocondi et al., 1997; Liu et al., 2005). It has been proposed that the large steps interact with unit screw dislocations and the heterogeneous phase to form the micropipe.

3.1.1 Experimental observations

Fig. 6a and 6c show the stress birefringence images of two typical micropipes with different diameters respectively. They look like butterflies with four bright wings, and have a dark core in the center. The wings' length varies with the diameter of micropipe. The wings' brightness was also not uniform from the center to the outside. The longer the distance from the center, the weaker is the brightness of the wings. Fig. 6b and 6d exhibit the bright field images of the two micripipes respectively. The open cores were visible distinctly in the centers of micropipes especially for the one with large diameter. When we rotated the sample, the birefringence pattern rotated simultaneously (as shown in Fig. 7).

3.1.2 Theoretical explanations

In this chapter we describe the strain field of a micropipe by the theory of screw dislocation. According to Frank's theory, micropipes are dislocations with large Burgers vectors. Therefore the strain field caused by the micropipes could be described by dislocation theory and stress birefringence image from a micropipe could be simulated. The existence of micropipes changes the crystal from uniaxial to biaxial crystal in the neighbour area of a micropipe.
So the interference intensity near a micropipe should be written as follows:

$$I = \begin{cases} (A / r^2)\sin^2(2\theta - 2\alpha) & \text{when } r > r_0 \\ 0 & \text{when } r < r_0 \end{cases} \tag{2}$$

where r_0 is the diameter of the micropipe, α is the angle between <2-1-10> direction and polarizer, A is constant which can be expressed as:

$$A = \frac{I_0 \cdot \mu^2 \cdot b^2 \cdot n^6 \cdot \pi_{44}^2 \cdot \Delta l^2 \cdot \cos^2 2\beta}{64\lambda^2} \tag{3}$$

When $r > r_0$, the contour equation of the intensity curve can be obtained

$$r^2 = \frac{I_0}{I} f^2 \sin^2(2\theta - 2\alpha)\mu m^2 \tag{4}$$

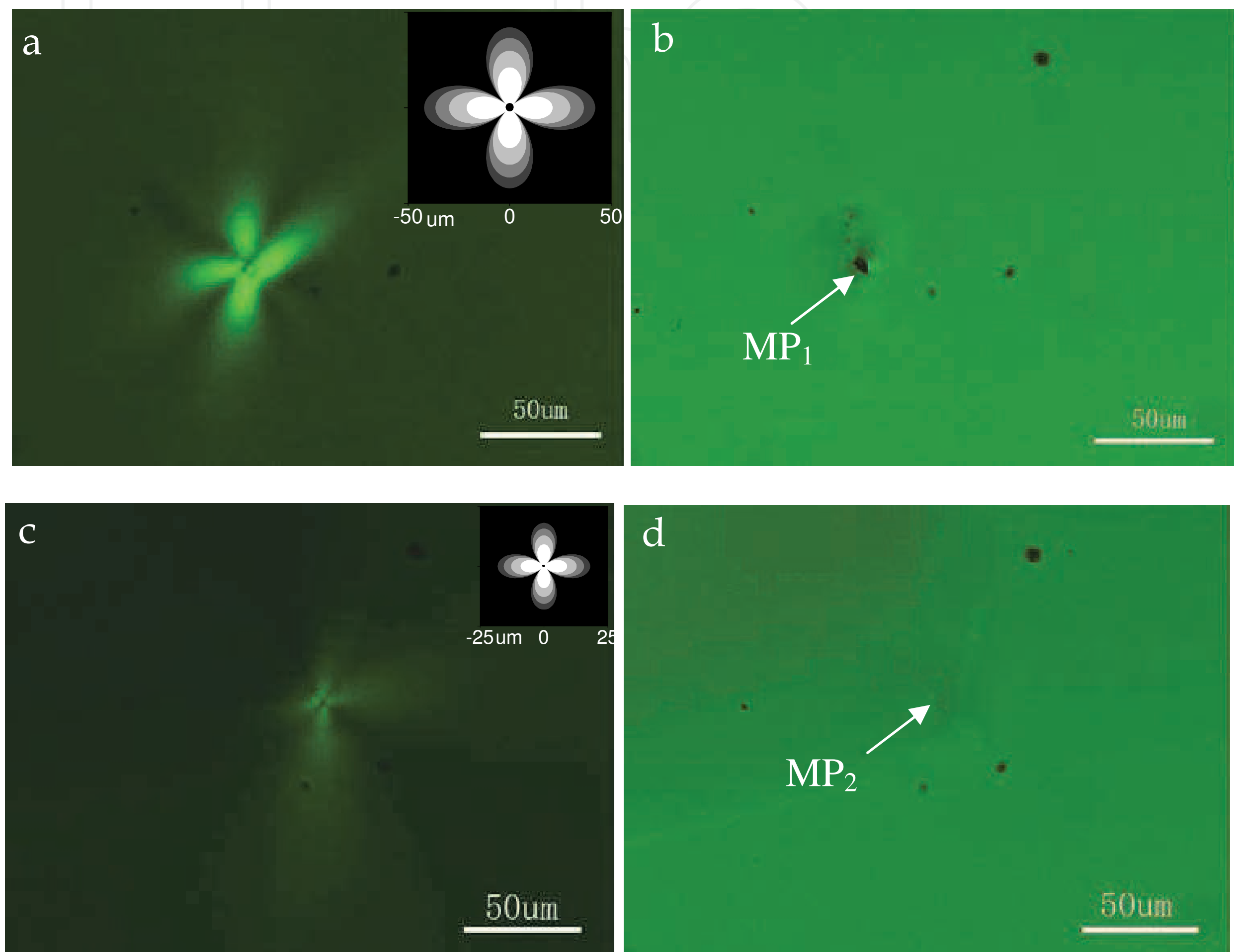

Fig. 6. Microscopic images of two micropipes (MP_1 and MP_2). (a) A unique interference pattern observed by a polarizing optical microscope for MP_1. (b) A bright-field optical microscopic image for MP_1. (c) A unique interference pattern observed by a polarizing optical microscope for MP_2. (d) A bright-field optical microscopic image for MP_2. Images (a) and (b) are the same micropipe with a larger Burgers vector; images (c) and (d) are the same micropipe with a smaller Burgers vector. The insets in the upper right of (a) and (c) give the simulation of MP_1 and MP_2, respectively. The black spots that appear in the four images are foreign particles on the lens.

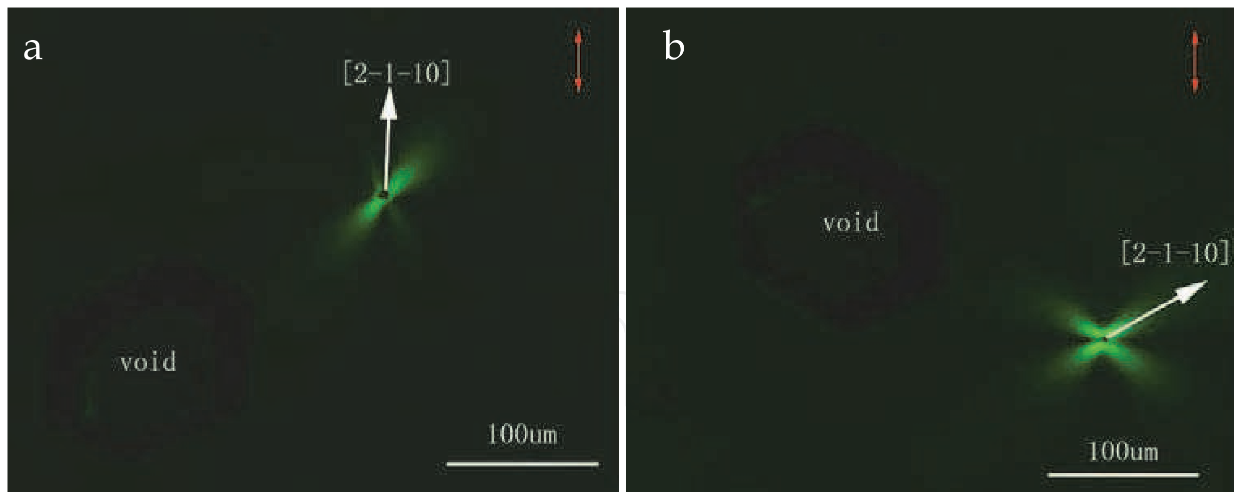

Fig. 7. Microscopic images of micropipe observed by a polarizing optical microscope with different α. The red and white arrows represent the directions of the polarizer and the <2-1-10> direction, respectively. (a) α =0. (b) α = π /4.

From Eq. 4, we can get interference intensity contours with different I_0/I, as shown in Fig. 6. The smaller the intensity of incident beam, the longer is the birefringence pattern's radius.
In Fig. 6 the diameters of MP_1 and MP_2 are about 4.0μm and 0.66μm. According to Eq. 1 and Eq. 4, the lengths of the brightest wings (in case of $I=I_0$) for the two micropipes could be calculated (Table 1). The observed and calculated values for these wings are nearly the same with two different micropipes. The insets in the upper rights of Fig. 6a and 6c give the simulation of MP_1 and MP_2 respectively. The simulation images are indeed a butterfly with four wings having a gradual changed intensity and a black core as same as the recorded images. However the four wings are not symmetrical in Fig. 6a. This may be caused by the off-orientation of the sample. The core of MP_1 is not circular in Fig. 6b, which can not happen in on-axis sample for the consideration of energy. This indicates the off-axis of the sample surface.
From Eq. 4, it is known that the birefringence images rotated with different α. For example, if we rotate the sample for π /4 (α= π /4), the equal interference intensity contours rotated for π /4. This result fit well with the experimental results shown in Fig. 7, where the red and white arrows represent the directions of the polarizer and <2-1-10> direction respectively. A void is taken as a reference point in Fig. 7. In Fig. 7a, <2-1-10> direction is parallel to the polarizer, the bright wings make an angle of π /4 with <2-1-10> direction. In Fig. 7b, <2-1-10> direction make an angle of π /4 with the polarizer, the bright wings make an angle of zero with <2-1-10> direction. We can conclude that the calculated rotation property also agreed with the experimental results.

MP	Observed core diameter (D)	length of the brightest wing (r)	
		Observed	Calculated
MP1	4.00μm	22.2μm	21μm
MP2	0.66μm	8.3μm	9μm

Table 1. The observed and calculated wing lengths of MP_1 and MP_2 in case of $I=I_0$

3.1.3 Evolution of micropipes during growth

Fig. 8 shows the microscopic images for the same area but in different growth stages of the same crystal. The micropipes' distribution proves that Fig. 8a and 8b, 8c and 8d are the same areas in different growth stages respectively. The diameter of the micropipe is increasing with the crystal growth which can be proved by the size of bright wings in the birefringence images. It means that the stress can be released through micropipes during cryatal growth.
According to statistic of the densities of micropie along crystal growth, the micropipe density decreased with growth process for almost all samples, except one. That is to say, in case of optimizing growth conditions, micropipe density can be decreased and crystal quality can be improved.

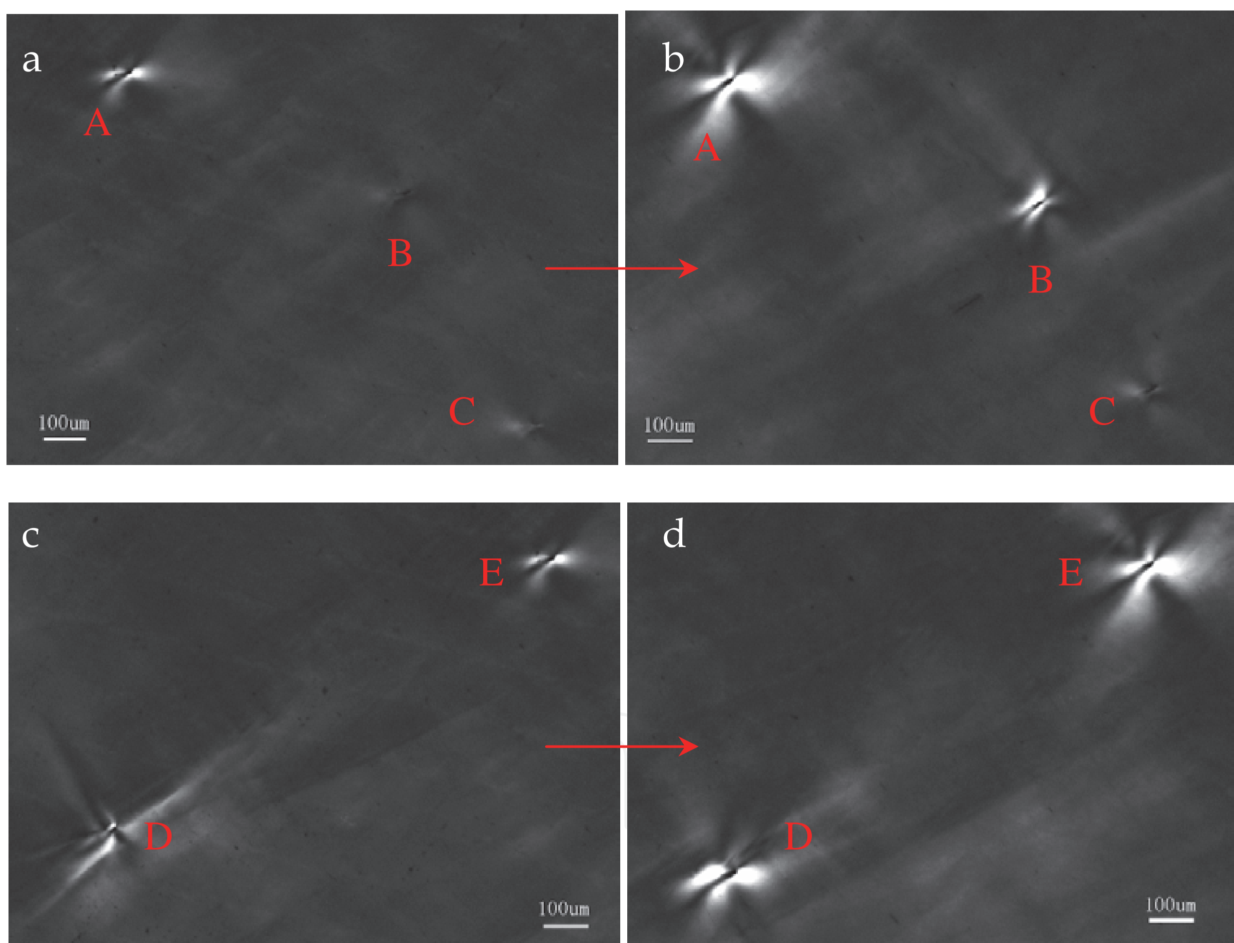

Fig. 8. Development of micropipes along growth direction, the red arrows represent the growth direction. Figure a and b belong to a same area; Fig. c and d belong to another same area.

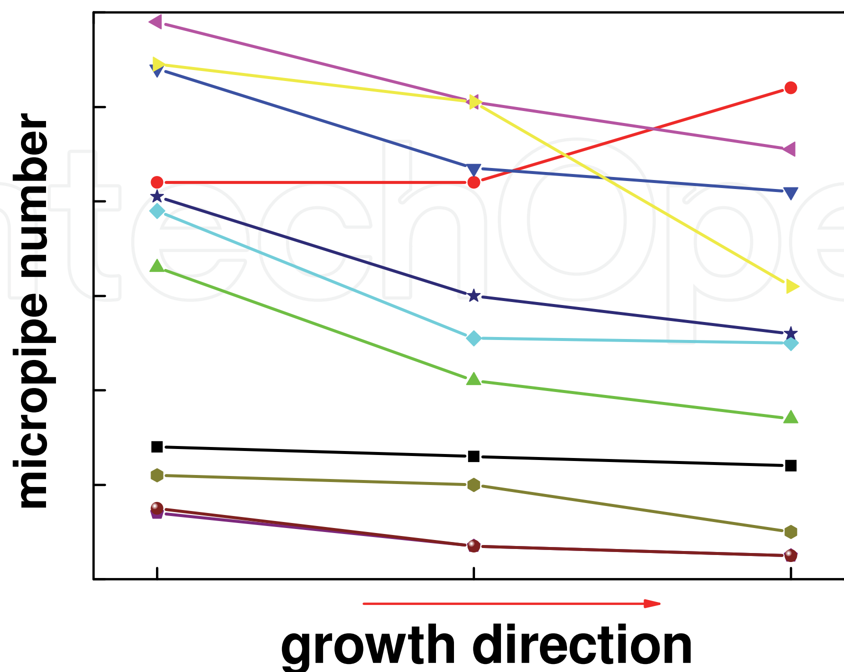

Fig. 9. Micropipes distribution along growth direction

3.1.4 Summary

In summary, the birefringence images of micropipes in 6H-SiC single crystals were observed by a polarization optical microscope. Based on the Frank's theory, the micropipes were treated as screw dislocations with huge Burgers vectors. Due to the strain caused by a micropipe, the SiC crystal in the neighbour area around a micropipe transferred from uniaxial into biaxial crystal. In the meanwhile, the refractive index ellipsoid was described by three principal refractive indexes and birefringence occurred. Based on above consideration, the birefringence images of micropipes with different Burgers vectors were simulated. The results agreed well with the observations. It confirms indirectly the Frank's theory that a micropipe is actually the super-screw dislocation with huge Burgers vector. With crystal growth, the micropipe density has a tendency of decrease and the diameter of micropipes can be enlarged for the stress release.

3.2 Elementary screw dislocations

Although the elementary screw dislocations did not seriously deteriorate the performance of device as micropipes, they prevent the realization of high-efficiency, reliable electronic devices (Lendenmann, 2001; Malhan et al., 2003; Neudeck et al., 1998).

In order to assess the density of elementary screw dislocation, back-reflection synchrotron radiation topograph of (0001) wafer was taken. In experimental setup, symmetric diffraction geometry with 000**30** reflection was used. The angle between incident beam and sample surface was 83°. In this case, the selected X-ray wavelength is 0.1nm. The distance between sample and film was 20cm. The illumination area is 1mm x 1mm.

Fig. 10 shows the back-reflection synchrotron radiation topograph of SiC (0001) wafer with 000**30** reflection. From the topograph, many white dots with the same diameters of 26-28μm can be observed. As the simulation results in following paragraphs, these white dots correspond to elementary screw dislocations. Therefore, the density of elementary screw dislocation in this wafer was measured to be $1.56\text{x}10^4/\text{cm}^2$.

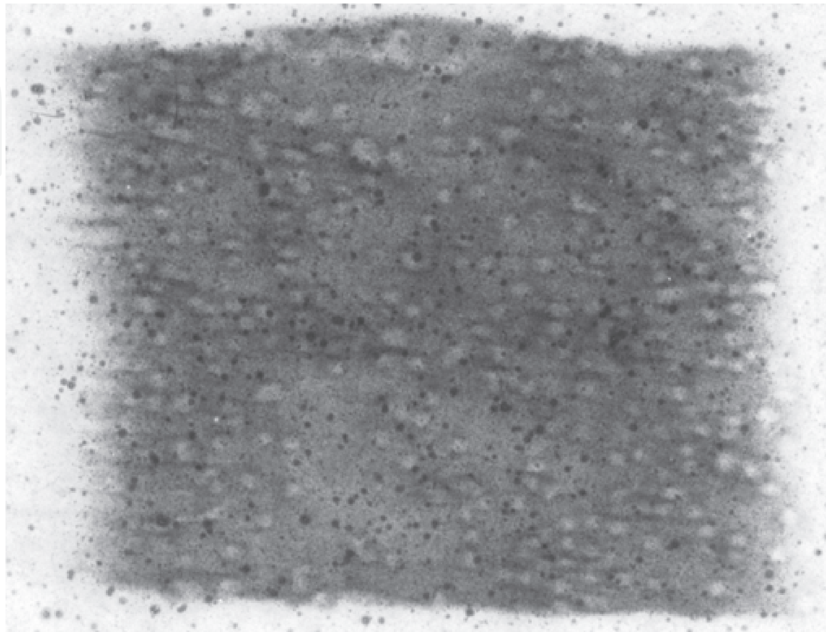

Fig. 10. Back-reflection synchrotron radiation topograph of SiC wafer with 000**30** reflection

The image of elementary screw dislocation can be simulated by ray-tracing method (Huang et al., 1999). As well known, for a screw dislocation along z axis, its displacement field can be described as

$$u_z = (b / 2\pi)\tan^{-1}(y / x) \tag{5}$$

Here b is the Burgers vector of screw dislocation. y and x are the coordinate position of arbitrary point in distorted area. From Eq. 5, the position-dependent orientation of the (0001) reflection plane can be expressed by the following equation.

$$\begin{aligned} n_x(x,y,z) &= by / r(b^2 + 4\pi^2 r^2)^{1/2} \\ n_y(x,y,z) &= -bx / r(b^2 + 4\pi^2 r^2)^{1/2} \\ n_z(x,y,z) &= 2\pi r / (b^2 + 4\pi^2 r^2)^{1/2} \end{aligned} \tag{6}$$

Where $r=(x^2+y^2)^{1/2}$. For the numerical simulation of the screw dislocation, the distorted lattice was divided into a set of small cubes of constant. All the cubes were assumed to have the same integrated diffraction density I_0. The recording plane was also divided into a set of squares of constant area. Then the intensities from all the cubes were projected to the corresponding squares according to the traces of the diffracted beams. The sum of intensities each square received after the projection represents the local contrast level. Eventually, all the calculated intensity can be plotted as a gray-scale topograph to give the simulation of the screw dislocation image.

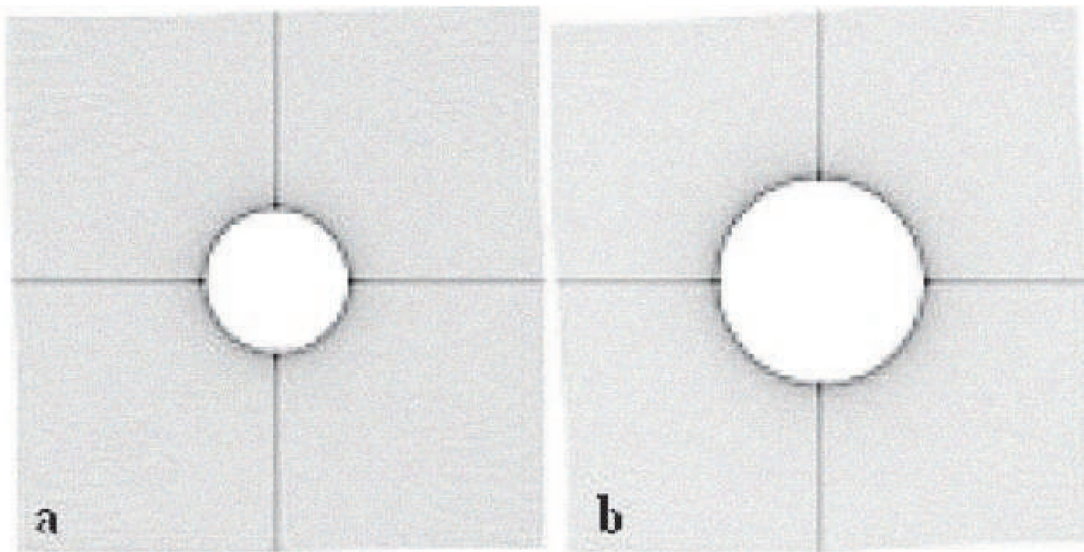

Fig. 11. The simulation images of screw dislocations with different Burgers vectors. (a). Elementary screw dislocation with Burgers vector 1c; (b). Screw dislocation with Burgers vector 2c. The image area is 100μm x l00μm.

Fig. 11a and 11b show the simulation images of an elementary screw dislocation with Burgers vector lc and a screw dislocation with Burgers vector 2c respectively. From the simulation images, the white dot diameter corresponding to an elementary screw dislocation with Burgers vector lc was measured to be 28μm. It is in well agreement with synchrotron observation. As for the screw dislocation with Burgers vector 2c, the corresponding white dot diameter from simulation was measured to be 39μm . Obviously, almost all the white dots in Fig. 10 correspond to elementary screw dislocations.

3.3 Basal plane bending

Recently, basal plane bending of SiC single crystals has attracted much attention (Lee et al., 2008; Seitz et al., 2006). In the case of basal plane bending, the normal orientation of the basal plane varies with the position from point to point. Basal plane bending causes serious lattice deformation and leads to the formation of low-angle boundaries. It was found that the degree of basal plane curvature in the facet region was less serious than that in the periphery region (Seitz et al., 2006). Therefore only the central part of a substrate can meet the requirements of device applications in the case of basal plane bending. For evaluating the crystal quality, <0001> orientated 6H-SiC samples were tested by HRXRD and SWBXT.
The HRXRD was conducted by XPERT-PRO diffractometer. The incident beam was adjusted by the beam conditioner of four Ge(022) collimated crystals so that the X-ray beam on the sample was accurately the Cu-Kα_1(λ=1.54056Å) radiation. The symmetrical diffraction geometry has been used in the measurement. The slits for the incident beam and detector are 0.5mm × 4mm and two degree respectively. The tube voltage and tube current are 40kV and 40mA respectively.
Several samples were investigated by transmission synchrotron topography performed at the 4W1A beam line of Beijing Synchrotron Radiation Laboratory. In our experiment, the electron energy of storage ring was 2.2GeV and the beam current was 80-100mA. Transmission synchrotron topographs were taken by transmission Laue geometry. The

samples were orientated with the (0001) surface perpendicular to the incident beam and the topographs were recorded by Fuji film.

3.3.1 Experimental results-HRXRD

Fig. 12 shows the plot of the relative ω_{006} rocking curve peak position as a function of the beam position across the diameters of a 2 inch wafer. The three groups of data in Fig. 12 were got from three different diameters of the same wafer. In case of precisely orientated crystal without any basal plane bending, ω is equal to Bragg angle. But the HRXRD test here is not the case. When the incident beam is located on the left of the center, the ω is larger than Bragg angle and the deviation of ω from Bragg angle is proportional to the distance between detected point and the center of the wafer. The farther the distance of the detected point from the center, the larger the deviation of surface from the basal plane. When the incident beam is located on the right of the center, the result is reversal, i.e. the ω is smaller than Bragg angle. The HRXRD experimental result implies that the (0001) basal plane in the sample is a concave face rather than a planar.

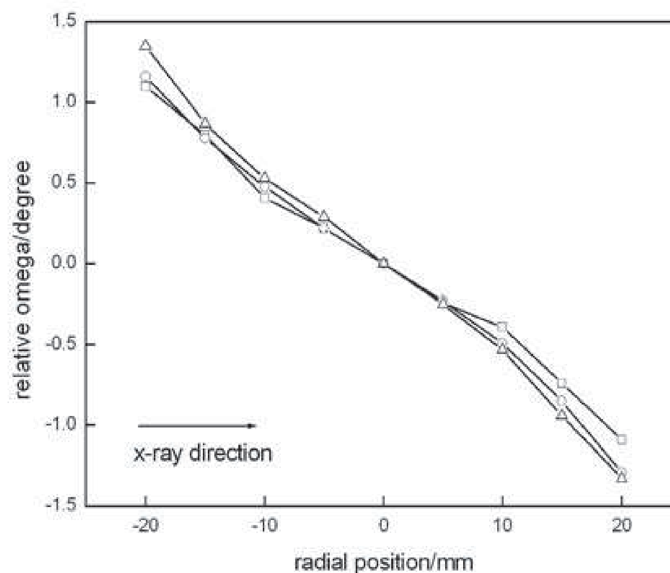

Fig. 12. Relative omega ($\Delta\omega_{006}$) peak position as a function of the beam position across the diameter of a 2 inch 6H-SiC wafer. The three lines were got from three different diameters on the same wafer.

3.3.2 Experimental results-SWBXT

The shape of the diffraction spots should be the same as that of footprint of X-ray source for a highly perfect crystal. In case of any lattice deformation, the diffraction spots for different reflections assume different shapes. Fig. 13 shows two transmission synchrotron topographs from two different samples. From this figure, it could be seen that the two samples have different distortion cases and each diffraction spot has its own shape in the two topographs. In Fig. 13a, all the diffraction spots are shrunk along the diffraction vector direction. In contrast, it seems that all the diffraction spots are stretched along the same line in Fig. 13b. No doubt, the two samples exist obviously structural imperfection. But is basal plane bending which causes the distortion of the diffraction spots?

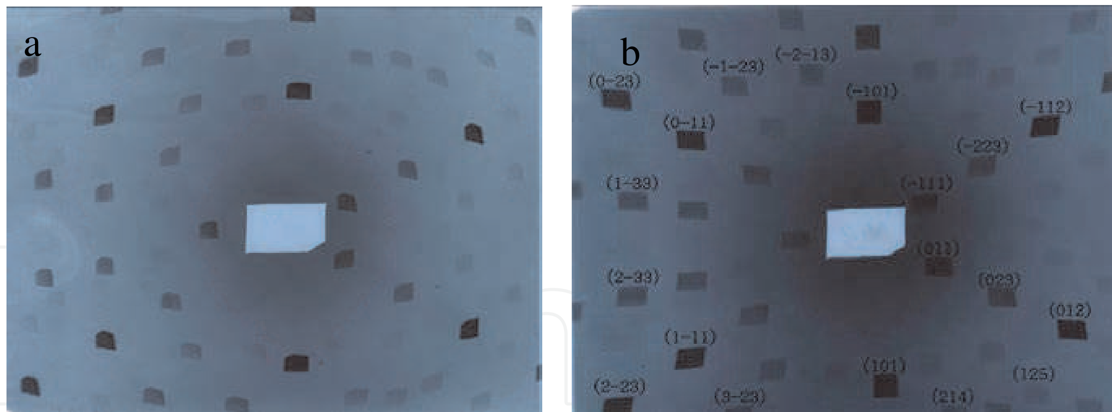

Fig. 13. Synchrotron white-beam transmission images for two different samples under the same experimental conditions.

3.3.3 Theory and simulation results for SWBXT

In order to explore the relationship between the distortion of the diffraction spots and lattice imperfection, the shapes of Laue spots have been simulated based on the (0001) Si face concave sphere model.

We establish two Cartesian systems X, Y, Z at sample (X and Y are parallel to the vertical and the horizontal base line respectively, Z is opposite to the incident X-ray direction, as shown in Fig. 14), which stands for the spatial system and X´, Y´, Z´ (X´, Y´ and Z´ are parallel to <10-10>, <-12-10> and <0001> direction respectively), which stands for the crystallophysical system. The unit vectors for X, Y, Z and X´, Y´, Z´ systems are $\vec{i}, \vec{j}, \vec{k}$ and $\vec{i}', \vec{j}', \vec{k}'$ respectively.

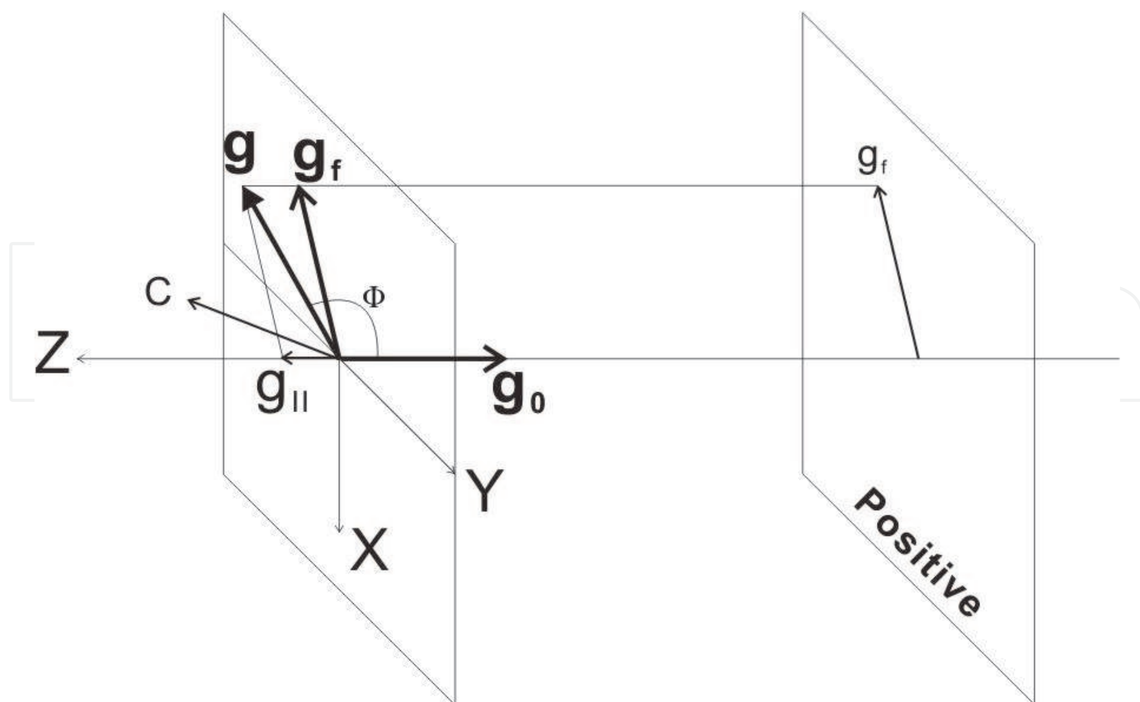

Fig. 14. Diffraction geometry of synchrotron white-beam topography in transmission mode. Where $\mathbf{g_0}$ is the incident unit vector; g is the diffraction vector; Φ is the angel between $\mathbf{g}$ and $\mathbf{g_0}$.

If the sample surface is exactly the (0001) plane, the two Cartesian systems coincide. Otherwise there will be a rotation for X´, Y´, Z´ system using X, Y, Z system as reference coordinate. Based on the HRXRD measurement, it is believed that the (0001) plane after bending is a concave sphere with a radius of R and only the center of the 2 inch wafer is exactly the (0001) plane. Here the center of 2 inch wafer is taken as the origin of the X, Y, Z system. Therefore the position of the spherical center is located at (0, 0, R). The c axis for an arbitary (x, y, 0) point on the sample surface deviates from the <0001> direction in case of basal plane bending. In other words, the Z´ directional vector at (x, y, 0) could be described as ($\cos\alpha$,$\cos\beta$,$\cos\gamma$) in X, Y, Z coordinate system, where

$$\cos\alpha = \frac{-x}{\sqrt{x^2+y^2+R^2}},\ \cos\beta = \frac{-y}{\sqrt{x^2+y^2+R^2}},\ \cos\gamma = \frac{R}{\sqrt{x^2+y^2+R^2}} \tag{7}$$

The directional vector from (0, 0, 0) to (x, y, 0) point could be written as ($\cos\delta$, $\sin\delta$, 0), where

$$\cos\delta = \frac{x}{\sqrt{x^2+y^2}},\ \sin\delta = \frac{y}{\sqrt{x^2+y^2}} \tag{8}$$

In case of basal plane bending, for an arbitary point (x, y, 0) on sample surface, a new system X´, Y´, Z´ is established. Such system is unique and has exclusiveness. The new system X´, Y´, Z´ is got from the rotation of X, Y, Z system around a defined axis in XY plane whose directional vector is ($\sin\delta$, $-\cos\delta$, 0). So the base vector transformation relationship between the two systems can be derived:

$$\begin{pmatrix} i' \\ j' \\ k' \end{pmatrix} = \begin{pmatrix} \cos^2\delta\cos\gamma+\sin^2\delta & \cos\delta\sin\delta\cos\gamma-\cos\delta\sin\delta & \cos\delta\sin\gamma \\ \cos\delta\sin\delta\cos\gamma-\cos\delta\sin\delta & \cos^2\delta+\sin^2\delta\cos\gamma & \sin\delta\sin\gamma \\ -\cos\delta\sin\gamma & -\sin\delta\sin\gamma & \cos\gamma \end{pmatrix} \begin{pmatrix} i \\ j \\ k \end{pmatrix} \tag{9}$$

In one setup of our experiment, the X-ray is perpendicular to the sample surface and parallel to <000-1> at central point of sample, i.e. the positive plane of (0001) is facing to the incident beam. Here we define the Laue image of (0001) wafer in such setup as positive image. Similarly the Laue image of (0001) wafer is defined as negative image when the (000-1) C-face is facing to the incident beam. So the incident unit vector $\mathbf{g}_0$ in positive image and the diffraction vector **g** for hkl reflection can be expressed as:

$$\mathbf{g}_0 = -\vec{k} \tag{10}$$

$$\mathbf{g} = h\mathbf{a}^* + k\mathbf{b}^* + l\mathbf{c}^* \tag{11}$$

where $\mathbf{a}^*$, $\mathbf{b}^*$ and $\mathbf{c}^*$ are reciprocal space base vectors. In X´, Y´, Z´ system, they can be expressed as follows:

$$\mathbf{a}^* = \frac{2}{\sqrt{3}a}\vec{i}\,',\mathbf{b}^* = \frac{1}{\sqrt{3}a}\vec{i}\,'+\frac{1}{a}\vec{j}\,',\mathbf{c}^* = \frac{1}{c}\vec{k}\,' \tag{12}$$

In case of basal plane bending, the crystallophysical system, X´, Y´, Z´, varies with sample position continuously. For analysis convenience, the diffraction vector **g** could be divided into two parts, projection of **g** on XY plane, i.e. $\mathbf{g}_f$ and projection of **g** on $\mathbf{g}_0$ direction. The following formula can be got in X, Y, Z system:

$$\begin{aligned}\mathbf{g}_f = &\left\{\left(\frac{2h}{\sqrt{3}a}+\frac{k}{\sqrt{3}a}\right)(\cos^2\delta\cos\gamma+\sin^2\delta)+\frac{k}{a}(\sin\delta\cos\delta\cos\gamma-\right.\\ &\left.-\sin\delta\cos\delta)-\frac{l}{c}\cos\delta\sin\gamma\right\}\vec{i}+\left\{\left(\frac{2h}{\sqrt{3}a}+\frac{k}{\sqrt{3}a}\right)(\sin\delta\cos\delta\cos\gamma-\right.\\ &\left.-\sin\delta\cos\delta)+\frac{k}{a}(\cos^2\delta+\sin^2\delta\cos\gamma)-\frac{l}{c}\sin\delta\sin\gamma\right\}\vec{j}\end{aligned} \tag{13}$$

If the angle between **g** and $\mathbf{g}_0$ is Φ, the diffraction angle θ can be written as follow according to their relationship in Fig. 14:

$$\sin\theta = -\cos\Phi = -\frac{B}{\sqrt{A}} \tag{14}$$

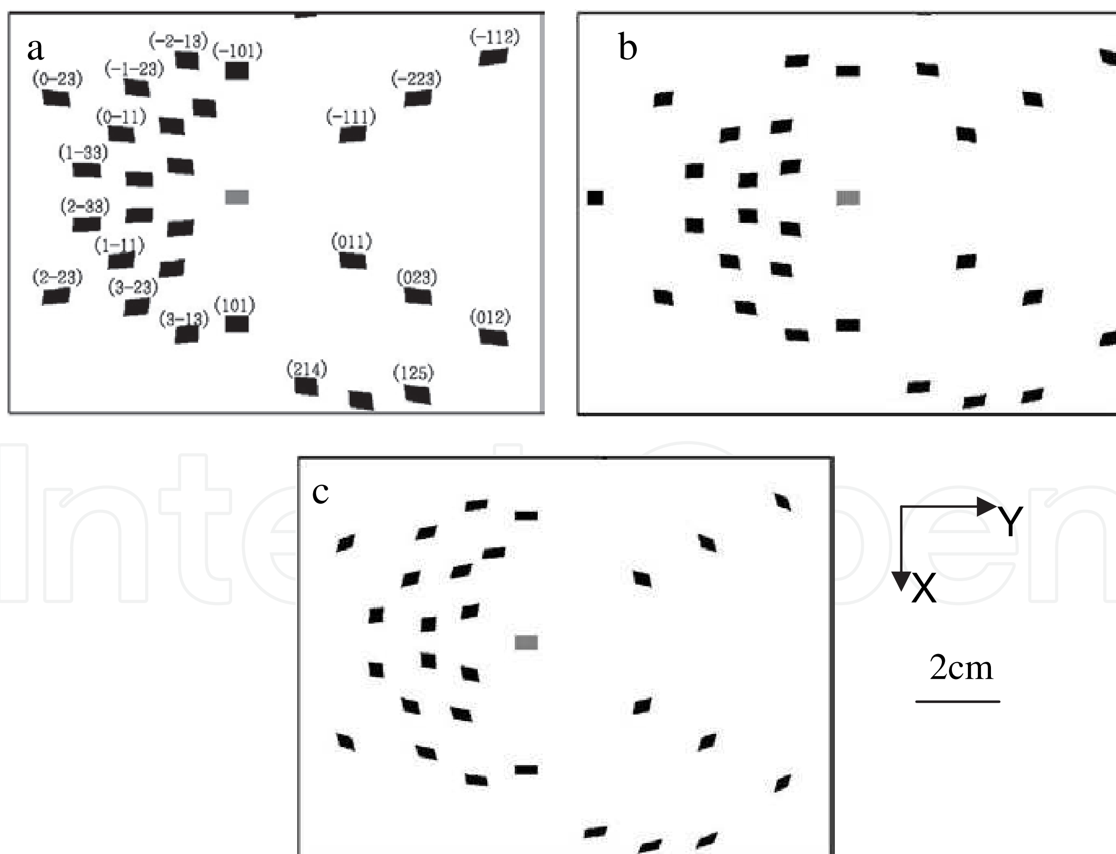

Fig. 15. The simulation results with conditions are as follows: light spot is 4mm × 6mm (the gray rectangle), D=10cm, a=0.3078nm, c=1.5117nm, $x_0 \in [-2, 2]$, $y_0 \in [-3, 3]$. (a) concave plane, R=100cm. (b) convex plane, R=100cm. (c) convex plane, R=60cm.

where

$$\begin{cases} A = (\frac{2h}{\sqrt{3}a} + \frac{k}{\sqrt{3}a})^2 + (\frac{k}{a})^2 + (\frac{l}{c})^2 \\ B = -(\frac{2h}{\sqrt{3}a} + \frac{k}{\sqrt{3}a})\cos\delta\sin\gamma - \frac{k}{a}\sin\delta\sin\gamma - \frac{l}{c}\cos\gamma \end{cases} \tag{15}$$

So the distance between the diffraction spots with the center spot on the positive image for hkl reflection, *d*, can be expressed as follow:

$$d = D \cdot tg2\theta = D \cdot \frac{-2B\sqrt{A - B^2}}{A - 2B^2} \tag{16}$$

where D is the distance between the sample and the film.
According to Eq. 13 and Eq. 16, the exact position of the diffraction spots on the positive image for hkl reflection can be determined. Moreover, for an arbitrary (x, y, 0) point on sample surface, its accurate positions for different reflections could be calculated.
According to the descriptions above, for an arbitrary reflection, the corresponding diffraction spot shape could be simulated. It was found that the shapes of diffraction spots depended on the diffraction vector, the basal plane bending radius and incident beam direction. In simulation, a 4mm × 6mm illumination area was given and the positions for 20 points along the periphery of illumination area with 1mm interval were calculated for different reflections. Finally from one to its neighbor point was connected for each reflection and a series of Laue spots with distortion shapes were obtained. The simulation results are shown in Fig. 15a when a concave surface of (0001) wafer faces to the X-ray. The shapes for five typical areas of a (0001) wafer were simulated, i.e. center region O and four different quadrant regions A, B, C and D. It was found that the diffraction spots' distortion did not show remarkably difference for the five different areas.
The simulations for (000-1) convex face, i.e. negative image were shown in Fig. 15b and 15c. The two images correspond to different curvature radiuses. It was found that the distortions of the Laue spots became more serious with a smaller curvature radius.
In SWBXT experiment, the area of footprint of X-ray area was 4mm × 6mm and the sample holder had a small rotation around X axis. The simulation ignored the holder rotation and diffraction intensity variations of different reflections. The above ignorance has no effect on distortion tendency of the Laue spots.
Sample 1 and 2 were etched, for the purpose of knowing their polarity (Si face or C face). From the etching results, it was known that the illuminated lattice plane for sample 1 and 2 are (000-1) and (0001) respectively. According to HRXRD results, (0001) plane is concave and (000-1) plane is convex. Therefore the illuminated lattice plane for sample 1 and 2 are convex and concave respectively.
Comparing the simulation results with the experimental observations, we can see obviously that Fig. 15b and Fig. 15a are nearly the same as Fig. 13a and Fig. 13b respectively. The main diffraction spots have the same distortion trend, which are shrunk and stretched along the diffraction directions respectively. When a convex lattice plane faces to x-ray source, its function is similar to a convex lens which make the X-ray focus and diffraction spots smaller. Similarly, the concave lattice face is like a concave lens, which make the X-ray defocus and diffraction spots larger.

3.3.4 Discussions

The HRXRD and SWBXT simulation results can confirm that basal plane bending exist in SiC single crystals. In SiC crystal growth experiments with different conditions, we found that the basal plane bending was caused mainly by the thermal mismatch between seed and holder which deteriorated the wafer's quality, i.e. increasing the density of low angle grain boundaries. Recently, the basal plane bending was eliminated by improving the seed attachment technique.

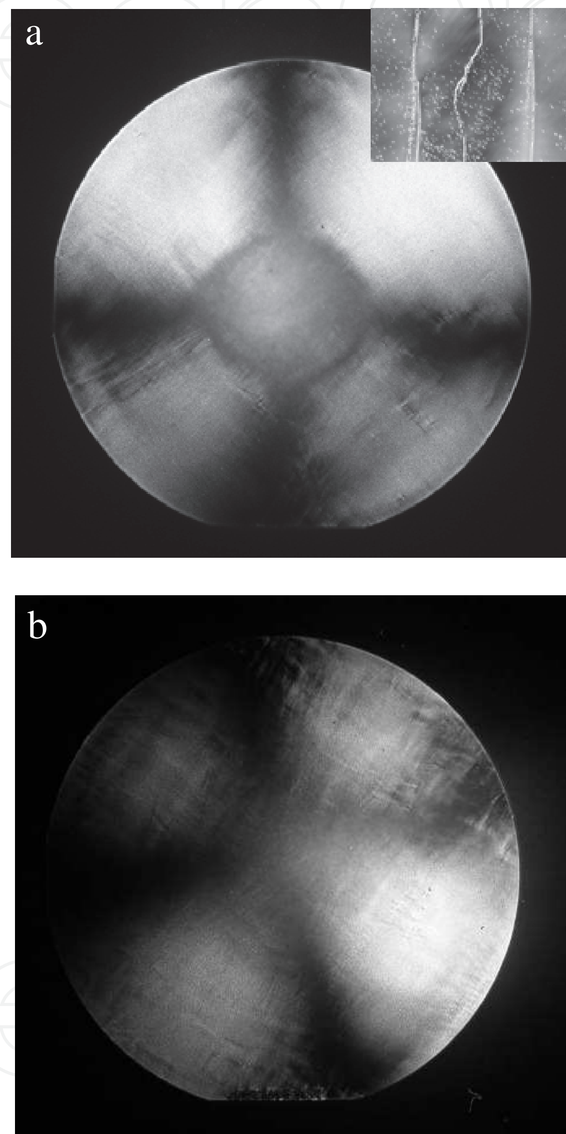

Fig. 16. Stress images for different wafers. The vertical directions <10-10>. (a) wafer with bending (The insert is a microscopic image of low angle grain boundaries after etching). (b) wafer without bending.

Fig. 16 are two stress images for two wafers grown with different conditions. The vertical direction is <10-10>. Fig. 16a stands for a wafer with basal plane bending. It can be seen obviously that there is a boundary between the center area (the facet) and the outside region. And a mass of low angle grain boundaries assembled along the <10-10> directions. The existance of grain boundaries deteriorated the crystal quality and reduced its usable

area. The insert of Fig. 16a is a microscopic image for <10-10> direction after etching. The white lines are low angle grain boundaries after etching. Fig. 16b stands for a wafer without basal plane bending. The boundary between the facet and the outside region disappeared. And the assembly of low angle grain bounbdaries along <10-10> direction disapppeared too. The stress for the whole wafer became more uniform. That is to say, the large number of grain boubdaries along <10-10> direction could be caused by basal plane bending.

4. Conclusion

In this chapter, polytype transition mechanism during 4H-SiC growth, the nature of micropipe and the existence of basal plan bending has been proposed. Elementary screw dislocations were also detected by back-reflection synchrotron radiation topography. All the results obtained above helped us to optimize the growth condition and then improve the crystal quality.

5. Acknowledgment

This work was supported by National Basic Research Program of China under grant No. 2009CB930503 and No. 2011CB301904, Natural Science Foundation of China under grant No. 51021062 and 50802053.

6. References

Lee, J. W. ; Skowronski, M. ; Sanchez, E. K. & Chung, G. (2008). Origin of basal plane bending in hexagonal silicon carbide single crystals, *Journal of Crystal Growth*, Vol. 310, No. 18, pp. 4126–4131, ISSN 0022-0248.

Lely, J.A. (1955). Darstellung von einkristallen von silicium carbid und beherrschung von art und menge der eingebautem verunreingungen, (in German). *Ber. Deut. Keram. Ges.*, Vol. 32, pp. 229-236.

Seitz, C. ; Herro, Z. G. ; Epelbaum, B. M. ; Hock, R. & Magerl, A. (2006). Lattice-plane curvature and small-angle grain boundaries in SiC bulk crystals, *Journal of Applied Crystallograohy*, Vol. 39, pp. 17–23, ISSN 0021-8898.

Hu, X. B. ; Xu, X. G. ; Li, X. X. ; Jiang, S. Z. ; Li, J. ; Wang, L. ; Wang, J. Y. & Jiang, M. H. (2006). Stacking faults in SiC crystal grown by spontaneous nucleation sublimation method, *Journal of Crystal Growth*, Vol. 292, pp. 192–196, ISSN 0022-0248.

Schulze, N. ; Barrett, D. L.; Pensl, G. ; Rohmfeld, S. & Hundhausen, M. (1999). Near thermal Equilibrium Growth of SiC by Physical Vapor Transport, *Materials Science and Engineering B*, Vol. 61-62, pp. 44-47, ISSN 0921-5107.

Straubinger, T. L ; Bickermann, M. ; Hofmann, D, ; Weingartner, R. ; Wellmann, P.J. & Winnacker, A. (2001). Stability Criteria for 4H-SiC Bulk Growth, *Materials Science Forum*, Vol. 353-356, pp. 25-28, ISSN 0255-5476.

Rost, H. ; Schmidbaner, M. ; Siche, D. & Fornari, R. (2006). Polarity- and Orientation-related Defect Distribution in 4H-SiC Single Crystals, *Journal of Crystal Growth*, Vol. 290, No. 1, pp. 137-143, ISSN 0022-0248.

Wang, L. ; Hu, X. B. ; Dong, J. ; Li, J. ;Jiang, S. Z. ; Li, X. X. ; Xu, X. G. ; Wang, J. Y. & Jiang, M. H. (2004). (in Chinese). Polytypes Identification of SiC Crystal by Micro-raman Spectroscopy, *Journal of Functional Materials*, Vol. 35, pp. 3400-3404, ISSN 1001-9731.

Wahab, Q. ; Ellison, A. ; Henry, A. ; Janzen, E. ; Hallin, C. ; Persio, J. D. & Martinez, R. (2000). Influence of epitaxial growth and substrate-induced defects on the breakdown of 4H–SiC Schottky diodes, *Applied Physics Letters*, Vol. 76, No. 19, pp. 2725–2727, ISSN 1077-3118.

Neudeck, P. G. & Powell, J. A. (1994). Performance limiting micropipe defects in silicon carbide wafers, *IEEE Electron Device Letters*, Vol. 15, No. 2, pp. 63–65, ISSN 0741-3106.

Frank, F. C. (1951). Capillary equilibria of dislocated crystals, *Acta Crystallographica*, Vol. 4, No. 6, pp. 497–501.

Liu, J. L. ; Gao, J. Q. ; Cheng, J. K. ; Yang, J. F. & Qiao, G. J. (2005). Model for micropipe formation in 6H-SiC single crystal by sublimation method, *Material Letters*, Vol. 59, pp. 2374–2377, ISSN 0167-577X.

Giocondi, J. ; Rohrer, G. S. ; Skowronski, M. ; Balakrishna, V. ; Augustine, G. ; Hobgood, H. M. & Hopkins, R. H. (1997). An atomic force microscopy study of super-dislocation/micropipe complexes on the 6H-SiC(0001) growth surface, *Journal of Crystal Growth*, Vol. 181, pp. 351–362, ISSN 0022-0248.

Neudeck, P. G. ; Huang, W. & Dudley, M. (1998). Breakdown degradation associated with elementary screw dislocations in 4H-SiC p+n junction rectifiers, *Solid-State Electron*, Vo1. 42, No. 12, pp. 2157-2164, ISSN 0038-1101.

Lendenmann, H. ; Dahlquist, F. ; Johansson, N. ; Soderholm, R, ; Nilsson, P.A. ; Bergman, J. P. & Skytt, P. (2001). Long term operation of 4.5kV PiN and 2.5kV JBS diodes, *Material Science Forum*, VoI.. 353-356, pp. 727-730, ISSN 0255-5476.

Malhan, R.K. ; Nakamura, H. ; Onda, S. ; Nakamura, D. & Hara, K. (2003). Impact of SiC structural defects on the degradation phenomenon of bipolar SiC devices, *Material Science Forum*, VoI. 433-436, pp.917-920, ISSN 0255-5476.

Huang, X.R. ; Dudley, M. ; Vetter, W. M. ; Huang, W. ; Si,W. & Carter Jr, C.H. (1999) Superscrew dislocation contrast on synchrotron white-beam topographs: an accurate description of the direct dislocation image, *Journal of Appllied Crystallography*, Vo1. 32, pp. 516-524, ISSN 0021-8898.

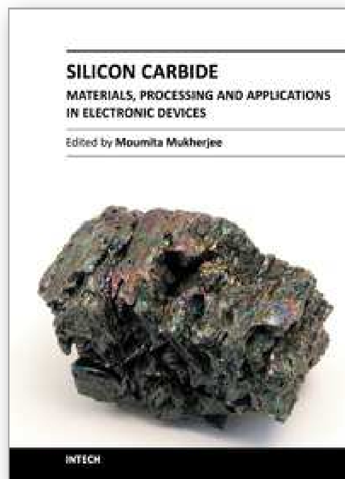

Silicon Carbide - Materials, Processing and Applications in Electronic Devices
Edited by Dr. Moumita Mukherjee

ISBN 978-953-307-968-4
Hard cover, 546 pages
Publisher InTech
Published online 10, October, 2011
Published in print edition October, 2011

Silicon Carbide (SiC) and its polytypes, used primarily for grinding and high temperature ceramics, have been a part of human civilization for a long time. The inherent ability of SiC devices to operate with higher efficiency and lower environmental footprint than silicon-based devices at high temperatures and under high voltages pushes SiC on the verge of becoming the material of choice for high power electronics and optoelectronics. What is more important, SiC is emerging to become a template for graphene fabrication, and a material for the next generation of sub-32nm semiconductor devices. It is thus increasingly clear that SiC electronic systems will dominate the new energy and transport technologies of the 21st century. In 21 chapters of the book, special emphasis has been placed on the â€œmaterialsâ€ aspects and developments thereof. To that end, about 70% of the book addresses the theory, crystal growth, defects, surface and interface properties, characterization, and processing issues pertaining to SiC. The remaining 30% of the book covers the electronic device aspects of this material. Overall, this book will be valuable as a reference for SiC researchers for a few years to come. This book prestigiously covers our current understanding of SiC as a semiconductor material in electronics. The primary target for the book includes students, researchers, material and chemical engineers, semiconductor manufacturers and professionals who are interested in silicon carbide and its continuing progression.

How to reference
In order to correctly reference this scholarly work, feel free to copy and paste the following:

Lina Ning and Xiaobo Hu (2011). Bulk Growth and Characterization of SiC Single Crystal, Silicon Carbide - Materials, Processing and Applications in Electronic Devices, Dr. Moumita Mukherjee (Ed.), ISBN: 978-953-307-968-4, InTech, Available from: http://www.intechopen.com/books/silicon-carbide-materials-processing-and-applications-in-electronic-devices/bulk-growth-and-characterization-of-sic-single-crystal

INTECH
open science | open minds

InTech Europe
University Campus STeP Ri
Slavka Krautzeka 83/A
51000 Rijeka, Croatia
Phone: +385 (51) 770 447
Fax: +385 (51) 686 166

InTech China
Unit 405, Office Block, Hotel Equatorial Shanghai
No.65, Yan An Road (West), Shanghai, 200040, China
中国上海市延安西路65号上海国际贵都大饭店办公楼405单元
Phone: +86-21-62489820
Fax: +86-21-62489821

www.intechopen.com

www.intechopen.com

© 2011 The Author(s). Licensee IntechOpen. This is an open access article distributed under the terms of the Creative Commons Attribution 3.0 License, which permits unrestricted use, distribution, and reproduction in any medium, provided the original work is properly cited.

IntechOpen

IntechOpen